JOURNAL OF SPACECRAFT AND ROCKETS
Vol. 46, No. 3, May–June 2009

Analysis of Space Shuttle Primary Reaction-Control Engine-Exhaust Transients

Benjamin D. Hester,* Yu-hui Chiu,† and Jeremy R. Winick‡
U.S. Air Force Research Laboratory, Hanscom Air Force Base, Massachusetts 01731
Rainer A. Dressler,§ Lawrence S. Bernstein,¶ and Matthew Braunstein**
Spectral Sciences, Inc., Burlington, Massachusetts 01803-3304
and
Paul F. Sydney††
Pacific Defense Solutions, Kihei, Hawaii 96753

DOI: 10.2514/1.39516

A series of 22 primary reaction-control-system engine attitude-control firings were observed from the Maui Space Surveillance Site during the space shuttle STS-115 mission. The firings occurred during a pass over Maui on 19 September 2006 during which the orbiter was in sunlight and the observatory was in darkness. The observed attitude maneuvers maintained the orbiter in an orientation in which its long axis was aligned with the line of sight from the observatory. This ensured that the thrust vectors of all the observed engine firings were perpendicular to the line of sight, providing an optimal side-on observation of the exhaust. The firings ranged between 80 and 320 ms in duration and involved 2 or 3 engines for pitch, roll, and yaw adjustments. A 0.328 deg field-of-view acquisition scope of the 3.6 m telescope of the Advanced Electro-Optical System provided unfiltered imagery in the near-ultraviolet visible spectral region. The most interesting white-light features were transients, one observed at engine start up and two at shutdown. The analysis of the transient speeds reveals that the startup transient consists of either unburned propellant droplets or higher-pressure gas evaporated from droplets and that the shutdown transients are attributable to a slightly staggered release of unburned oxidizer and fuel, respectively. The first (oxidizer) shutdown transient is the brightest feature, for which an intensity evolution analysis is conducted. The analysis of the ground-based data is fully consistent with spectral features attributable to primary reaction-control-system engine transients observed in previous measurements from the space shuttle bay using an imager spectrograph.

Nomenclature

A	=	Brook scaling parameter for density, cm^{-1}
A	=	Brook scaling parameter for flux, g
A'	=	Lorentzian scaling parameter for density, $\text{cm}^{-1} \cdot \text{deg}^2$
A'	=	Lorentzian scaling parameter for flux, $\text{g} \cdot \text{deg}^2$
B	=	Brook angular distribution parameter, unitless
C_p	=	specific heat at constant pressure, $\text{J} \cdot \text{g}^{-1} \cdot \text{K}^{-1}$
D	=	particle diameter, μm
D_0	=	initial particle diameter, μm
d	=	horizontal video-image frame width at range, R, km
F	=	exhaust particle flux, $\text{cm}^{-2} \cdot \text{s}^{-1}$
$F_S(\nu)$	=	solar spectral flux, $\text{W} \cdot \text{cm}^{-2}$
$g(\nu)$	=	spectral atmospheric transmission and sensitivity factor, unitless
$I(R_e, x)$	=	radiant intensity along image coordinate x perpendicular to the thrust axis at nozzle distance R_e, $\text{W} \cdot \text{cm}^{-2}$
$I(R_e, y)$	=	volume emission rate at nozzle distance R_e, where y is the radial distance with respect to the thrust axis, $\text{W} \cdot \text{cm}^{-3}$
$I(\theta)$	=	angular volume emission-rate distribution, $\text{W} \cdot \text{cm}^{-3}$
$I(\varphi)$	=	scattered intensity as a function of the solar scattering angle, $\text{W} \cdot \text{sr}^{-1}$
m	=	particle mass, g
N	=	number density, particles cm^{-3}
$P(\nu, T)$	=	Planck radiation function, $\text{W} \cdot \text{sr}^{-1} \cdot \text{cm}^{-2} \cdot \text{Hz}^{-1}$
P_{vap}	=	vapor pressure, torr
Q	=	heat gain rate, W
Q_{Earth}	=	Earthshine heating rate, W
Q_{rad}	=	radiative cooling rate, W
Q_{sub}	=	heat of sublimation cooling rate, W
Q_{sun}	=	solar radiation heating rate, W
R	=	range, km
$\mathbf{R}$	=	range vector, km
R_e	=	axial distance to the nozzle exit, m
r	=	particle radius, μm
T	=	temperature, K
$\mathbf{v}$	=	orbiter velocity vector, $\text{km} \cdot \text{s}^{-1}$
v	=	magnitude of the orbiter velocity vector, $\text{km} \cdot \text{s}^{-1}$
v_e	=	far-field exhaust velocity, $\text{km} \cdot \text{s}^{-1}$
$v_\perp$	=	projection of the orbiter velocity vector onto the image plane, $\text{km} \cdot \text{s}^{-1}$
x	=	image coordinate, m
y	=	radial distance with respect to the thrust centerline, m
z	=	distance along the orbiter z axis, m
α	=	elevation, deg
Γ	=	full width at half-maximum of the Lorentzian angular distribution, deg
γ	=	angle between the orbiter axis, z, and $\mathbf{R}$, deg
ΔH_{sub}	=	heat of sublimation, $\text{J} \cdot \text{g}^{-1}$

Received 2 July 2008; accepted for publication 1 October 2008.

*Space Scholar, Space Vehicles Directorate; currently Department of Mathematics and Statistics, Arizona State University, Tempe, AZ 85287-1804.
†Task Scientist, Space Vehicles Directorate. Member AIAA
‡Task Scientist, Space Vehicles Directorate.
§Principal Scientist, 4 Fourth Avenue. Member AIAA.
¶Chief Scientist, 4 Fourth Avenue.
**Group Leader, Computational Physics and Chemistry, 4 Fourth Avenue.
††Staff Scientist.

$\varepsilon(r, \nu)$ = size and frequency-dependent emissivity of a particle, unitless
θ = angle inscribed by the particle trajectory and thrust axis, deg
ν = radiation frequency, s^{-1}
ρ = mass density, $g \cdot cm^{-3}$
$\sigma(\nu, r, \varphi)$ = Mie-scattering differential cross section, $cm^2 \cdot sr^{-1}$
ϕ = solar phase angle, deg
φ = solar scattering angle, deg
Ω = solid angle, sr

Introduction

THE gaseous and condensed effluents from spacecraft engine firings can be a source of significant contamination for sensitive surfaces on spacecraft. This is particularly problematic in the case of large low-Earth-orbit space structures that require powerful propulsion systems for orbit maintenance and attitude control, such as the space shuttle and the International Space Station (ISS). Modeling of contaminant fluxes is necessary to optimize the design and integration of spacecraft subsystems and instruments. The models require precise information on exhaust constituents and their angular distribution. Condensed exhaust matter is a primary concern because of the high velocity of exhaust impacts and the chemically sensitive nature of optical surfaces.

Instruments on the ISS are exposed to contamination by service vehicles, including the space shuttle, Progress, Soyuz, and the ESA automated transfer vehicle during docking and separation maneuvers. A series of experiments have investigated contamination caused by space shuttle reaction-control-system engine exhaust [1,2]. The experiments measured deposition rates and clearly identified significant surface erosion, as evidenced by microcrater formation attributed to hypervelocity impacts by condensates in the exhaust. The measurements were only conducted on the thrust centerline, and therefore the deposition rates from these bipropellant engines as a function of angle with respect to the thrust axis are not known.

The STS-115 mission in September 2006 provided a valuable opportunity to examine condensed exhaust species, including angular distributions, during a terminator pass over the Maui Space Surveillance Site (MSSS). A set of dedicated burns was planned as part of the U.S. Air Force Research Laboratory Maui Analysis of Upper-Atmospheric Injections (MAUI) experiment. Because the unique lighting conditions (orbiter in sunlight and observatory in darkness) were optimal for imaging, and because there was concern over the possibility of having lost the parachute hatch, the flight officer canceled the dedicated MAUI burns and ordered an imaging overflight during which the shuttle's long axis was aligned with the line of sight of the MSSS telescope (landmark mode). Although unintended, the requirement to maintain a fixed attitude with respect to the observatory resulted in a long series of attitude-control firing bursts. This provided an unprecedented opportunity to acquire video imagery of sunlight scattering by exhaust condensed matter during a large number of engine startups and shutdowns.

The purpose of the present study was to derive condensate speeds and angular fluxes from remote observations of sunlight scattering from transient condensate clouds. The current paper presents an analysis of transients observed for a total of 22 attitude-control burns involving 2 or 3 primary reaction-control-system (PRCS) engines. These are the most frequently used space shuttle engines during ISS proximity. For each burn, 3 transients were identified, and the speeds of the center of the observed features could be accurately determined. The retrieved speeds allowed the determination of the ejection times of the matter causing the transients and their association with engine startup or shutdown. For the first time, angular distributions determined from the transverse intensity profiles of the transient clouds are reported. We have also conducted an analysis of the evolution of the integrated intensity of the most intense transient for each burn, which we attribute to pure oxidizer condensates. The observations are compared with model calculations of Mie-scattering intensities from condensed sublimating propellant particles. We also relate the present observations to previously unreported spectra associated with particle scattering observed following engine burns in sunlight using the Arizona Airglow Instrument (GLO) [3,4] imager spectrograph flown in the shuttle bay during STS-63.

Experimental

STS-115 on *Atlantis* was launched on 9 September 2006. The observation pass occurred on 19 September 2006 following undocking from the ISS. Culmination with respect to the observatory at MSSS was at 15:29:48 h coordinated universal time (UTC). Figure 1 provides a summary of pass parameters as a function of time, including range **R**, elevation α, solar phase angle ϕ, and the angle γ between the orbiter axis z and **R**. The geometry of the experiment and associated parameters are shown schematically in Fig. 2. The space shuttle flew over Hawaii in a landmark mode in which the orbiter z axis was oriented parallel to the line of sight such that high-resolution imagery could be acquired of the shuttle aft section. The burns that are the subject of this work were a series of attitude maneuvers fired perpendicularly to the orbiter z axis to maintain landmark mode. The bottom chart in Fig. 1 provides markers at the time of those attitude-control maneuvers. The time interval during

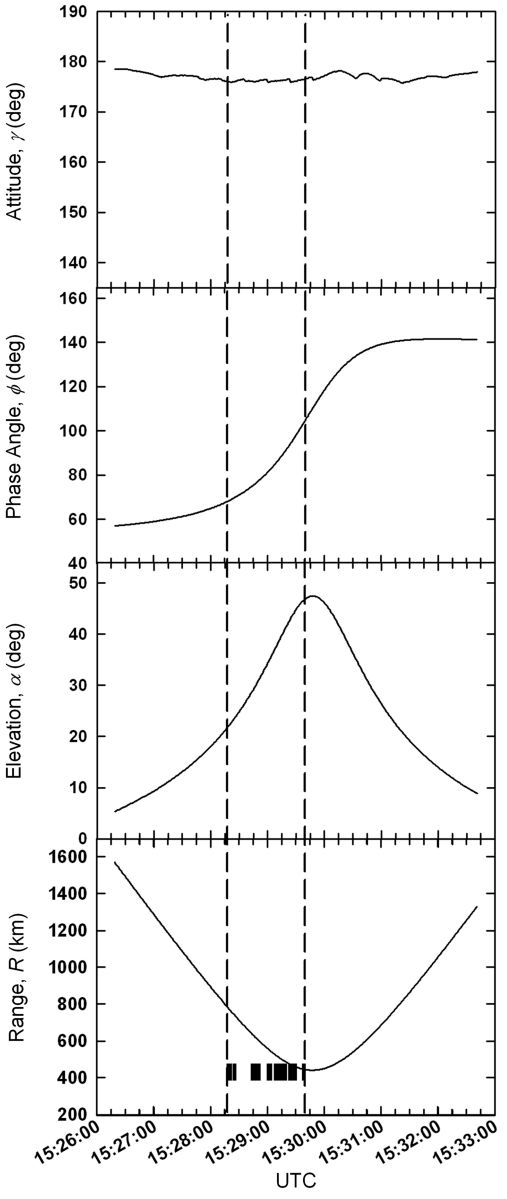

Fig. 1 Observational parameters during the 19 September 2007 pass of Atlantis over Maui.

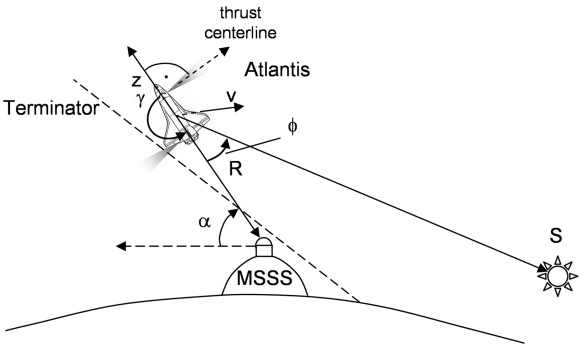

Fig. 2 Schematic representation of the observation geometry.

which quality imaging of burns could be acquired is indicated with vertical dashed lines. After 15:29:40 h, cirrus clouds caused significant background radiation as MSSS approached sunrise, substantially reducing the quality of the observations. The orbiter velocities in the Earth-centered-inertial (ECI) and Earth-centered-fixed coordinate systems were 7.715 and 7.42 km $\cdot$ s^{-1}, respectively. The orbital altitude was 335.15 ± 0.20 km within the time interval of the investigated burns, with **R** declining from 780 to 446 km during the approach. As shown in Fig. 1, during the investigated burn interval, the angle γ remained nearly constant at a value of 176.3 deg to within 0.5 deg. The minor discrepancy with a perfect alignment has minimal bearing on the present analysis.

Wide-field-of-view (FOV) imagery of the space shuttle maintaining axial alignment with the MSSS line of sight was obtained using the large-aperture acquisition telescope (LAAT). This 0.58-m-aperture telescope, situated on the advanced electro-optical system mount, was operated with a nominal FOV of 0.328 deg. The intensified-charge-coupled-device (ICCD) detector exhibits sensitivity in the spectral range of 0.4 to 0.9 μm. The sensor gain was set to limit the size of the spot attributable to saturation by the solar-illuminated orbiter hard body. Unfortunately, a sensitivity calibration was only conducted for a configuration involving filtered imagery with a different gain setting. The change to imaging experiments came so late that calibration measurements could not be conducted for the reduced-gain setting of the LAAT sensor.

Table 1 lists the pertinent parameters for 22 attitude-control burns for which quality (30 frames per second) video footage was obtained. Most of the burns were the minimum burn length of 0.08 s. Burns 2 and 8 were 0.16 s long, and burn 9 was 0.24 s long. Three types of attitude-control maneuvers actuating 2 or 3 PRCS engines were conducted: pitch down, roll left, and yaw right. The F1U, L3D, and R3D engines were used for pitch down; the L1U and R3D engines were used for roll left; and the F3L and R1R engines were used for yaw right. The thrust axis for all of these engines is perpendicular to the shuttle axis and is therefore essentially perpendicular to the line of sight, providing a side-on view of the engine exhaust. A space shuttle PRCS engine has a nominal thrust of 3880 N (870 lbf) and uses a monomethyl-hydrazine (MMH) fuel and N_2O_4 oxidizer.

Table 1 also lists the projection $v_\perp$ of the orbiter ECI velocity vector **v** onto the plane normal to the line of sight. This projection is directly proportional to the angular velocity of stars streaking across the FOV as the orbiter is tracked and is given by

$$v_\perp = v \sin(\angle\{\mathbf{R}, \mathbf{v}\}) \tag{1}$$

The dimensions of the video frame at the orbiter altitude can therefore be calibrated by determining the velocity of the star streaks in units of pixels per unit time, from which the scaling factor (distance per pixel) can be derived. This approach neglects a relatively insignificant contribution due to the motion of the Earth. At the small nominal FOV of 0.328 deg, it is within the accuracy of the present analysis to assume $\tan(\text{FOV}) \approx \text{FOV}$, thereby allowing the use of planar geometry for the image analysis. Table 1 lists the derived horizontal frame widths d, which vary from $\sim$3–5 km, versus orbiter distance. From $\text{FOV} = d/R$, we derive an average FOV of 0.374 deg for the 22 burns with a small standard deviation of 0.004 deg, thereby confirming a consistent calibration of the observed video imagery.

The present analysis of STS-115 observations is complemented by spectral measurements conducted with the GLO imager spectrograph flown earlier on STS-63. The GLO spectral measurements are reported here for the first time. The spaceborne GLO instrument has been described in detail before [3,4], including GLO measurements of engine-exhaust interactions with the upper atmosphere reported by Bernstein et al. [5,6]. GLO was mounted in the rear section of the shuttle bay. It comprises a nine-section spectrograph, three monochromatic imagers, and a TV camera, all boresighted to view in the same direction. The spectrograph and imagers have ICCD focal-plane detectors. The nine slightly overlapping spectrograph sections permit simultaneous recording of the spectrum from 115.0 to 900.0 nm with a spectral resolution of about 4 to 10 Å. Their combined focal-plane image is 4500 pixels wide in the wavelength (dispersion) dimension, perpendicular to the slit, and 192 pixels in the spatial dimension, along the slit. The slit image at the detector is a narrow portion of the image of the distant object being observed, preserving spatial resolution in the slit-length direction. The design

Table 1 List of PRCS engine burns analyzed in this work

Burn no.	UTC	Maneuver	Burn length, s	Range, km	$v_\perp$, km/s	d, km
1	15:28:18.993	Pitch down	0.08	778.837	4.607	4.976
2	15:28:21.073	Yaw right	0.16	766.504	4.670	4.924
3	15:28:25.473	Pitch down	0.08	740.743	4.809	4.770
4	15:28:44.593	Pitch down	0.08	635.166	5.508	4.137
5	15:28:45.313	Pitch down	0.08	631.436	5.537	4.113
6	15:28:48.353	Yaw right	0.08	615.922	5.663	3.990
7	15:28:51.073	Yaw right	0.12	602.383	5.779	3.914
8	15:29:00.673	Pitch down	0.16	557.521	6.203	3.665
9	15:29:02.673	Roll left	0.24	548.819	6.294	3.567
10	15:29:03.073	Roll left	0.08	547.108	6.312	3.551
11	15:29:08.673	Pitch down	0.08	524.242	6.568	3.442
12	15:29:12.193	Pitch down	0.08	510.990	6.726	3.342
13	15:29:14.113	Roll left	0.08	504.157	6.812	3.257
14	15:29:16.033	Roll left	0.08	497.619	6.896	3.251
15	15:29:16.593	Yaw right	0.08	495.768	6.920	3.250
16	15:29:18.993	Pitch down	0.08	488.141	7.021	3.181
17	15:29:23.713	Pitch down	0.08	474.638	7.209	3.105
18	15:29:26.193	Roll left	0.08	468.385	7.300	3.067
19	15:29:27.553	Roll left	0.08	465.215	7.347	3.088
20	15:29:29.473	Pitch down	0.08	461.060	7.410	3.047
21	15:29:38.313	Pitch down	0.08	447.029	7.630	2.940
22	15:29:39.073	Roll left	0.08	446.231	7.643	2.833

of the slit and fore optics affords a field of view of 0.2×8.5 deg. In the GLO measurements, the instrument was pointed almost parallel to the thrust axis of a PRCS engine. This orientation allowed the observation of far-field exhaust radiance while avoiding radiance due to the hot near-field vacuum core. Data acquisition and downloading are described in separate publications [7,8].

Results

Close inspection of the video imagery leads to the observation that 3 transients accompany every burn; this is demonstrated for burn 17 in Fig. 3. As we will show, the first transient is associated with engine startup, and the second and third transients are associated with engine shutdown. At the time of burn 17, the horizontal width of the frame corresponded to 3.105 km at the range of the orbiter, which is at the center of the circular region of saturated pixels. Stray light due to the intense sunlight scattered off the body of *Atlantis* caused significant blooming. The sharp streaks are stars, one of which was used for the frame-width calibration. Burn 17 was a pitch-down burn, which involves the two aft engines L3D and R3D firing downward and the forward engine F1U firing upward (toward the bottom right corner of the image) in the shuttle frame of reference. The first transient is the dimmest and has the highest velocity with respect to the shuttle. The second transient is the brightest and most compact, and the third has the lowest velocity and forms a trail due to a slow tail-off in the expelled material following the initial burst. The imagery also shows that there is considerable interaction between the visible exhaust features of the two aft engines.

The velocities of the individual transients were analyzed for every burn and engine by recording the time dependence of the distance of the point of highest intensity of the respective feature from the center of the orbiter along the exhaust centerline. A frame-by-frame analysis established that the transient velocities are constant with respect to the distance of the visual center of the feature to the orbiter. Thus, there is no effect due to interaction with the upper atmosphere, which is not surprising given the low thermospheric densities at 330 km during the near solar-minimum conditions of the experiment.

The analysis of the velocities is summarized in Table 2, in which the average transient velocities are sorted by engine and transient. The global averages of transient velocities averaged over all 22 burns are also provided. There are no noteworthy differences between the engines, the respective average values lying close to the standard deviations of the global average for a respective transient. The first transient has an average velocity of 3.13 ± 0.19 km $\cdot$ s^{-1}, close to

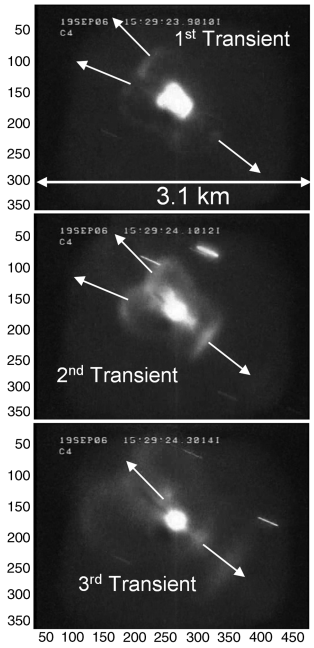

Fig. 3 Video frames separated by 0.2 s of burn 17.

Table 2 Axial transient velocities in km $\cdot$ s^{-1} determined for burns listed in Table 1.

Engine	Transient 1	Transient 2	Transient 3
F1U	3.268 ± 0.105	1.599 ± 0.067	0.795 ± 0.093
L3D	3.190 ± 0.172	1.686 ± 0.225	0.655 ± 0.143
R3D	3.078 ± 0.170	1.679 ± 0.172	0.701 ± 0.152
F3L	3.093 ± 0.175	1.485 ± 0.097	0.631 ± 0.051
R1R	3.348 ± 0.080	1.392 ± 0.146	0.675 ± 0.090
L1U	2.941 ± 0.205	1.527 ± 0.086	0.713 ± 0.033
Transient Average	3.132 ± 0.185	1.630 ± 0.175	0.707 ± 0.128

the terminal exhaust velocity of a PRCS engine [9,10]. The average velocity of transient 2 of 1.63 ± 0.18 km $\cdot$ s^{-1} is approximately half the velocity of transient 1, and transient 3 has an average velocity of 0.71 ± 0.13 km $\cdot$ s^{-1}, approximately half that of transient 2. No noticeable trend with time of burn is observed, and therefore effects due to engine heating on the terminal velocities can be excluded. Having derived the average velocities of the transients, the precise time of origin of the transients could be determined. The times of origin of transient 1 are identical to the engine startup time, and the times of origin of transients 2 and 3 are essentially the same and occur later. The intervals between the origin times of transient 2 and 3 and engine startup agree closely with the burn times reported to us by NASA. Consequently, transients 2 and 3 can be linked to engine shutdown.

Figure 4 shows intensity profiles through the transient images of the F1U engine shown in Fig. 3. Each pixel unit corresponds to 6.47 m. Profiles transverse to the thrust axis provide information on the angular flow distribution of the respective transient. The top figure is a transverse profile of transient 2 at the time of the center frame in Fig. 3. The data are compared with a Gaussian fit to the data, allowing for an offset with respect to background and maximum. It is seen that a Gaussian is a good representation of the distribution. In the central plot of Fig. 4, a transverse profile of transient 3 is shown, as observed in the bottom frame of Fig. 3. In this case, a Lorentzian provides a significantly improved fit. The bottom plot in Fig. 4 is a longitudinal profile taken from the bottom frame in Fig. 3, running from the orbiter position along the F1U thrust centerline. The longitudinal plot has been corrected with respect to background, as derived from the fits in the top 2 plots of Fig. 4. The background is consistently found to be approximately 50 intensity units. The intensity scale spans 256 units, and a nonlinear intensity regime must be assumed as the maximum intensity is approached. The orbiter presents the most intense saturated feature at around 200 intensity units. Both the second and third transients of the F1U engine can be identified as peaks in the profile. It is also apparent that there is some overlap between the two features.

The angular distribution of the exhaust transient constituents are obtained from the images in Fig. 3 by applying an Abel transformation [11] to a series of slices through the transient cloud transverse to the thrust axis at equally spaced axial distances to the nozzle exit, R_e. We assume that the feature is optically thin and axially symmetric. The transformation converts the relative radiant line-of-sight intensity distributions $I(R_e, x)$, where x is the image coordinate transverse to the thrust axis, to radial volume emission-rate distributions $I(R_e, y)$, where y is the radial distance with respect to the thrust centerline. The angular volume emission-rate distribution $I(\theta)$ averaged over the R_e interval of the selected slices is then obtained by using an angular binning approach across all points $I(R_e, y)$ of the Abel-transformed cloud with the relationship

$$\theta = \tan^{-1}(y/R_e) \tag{2}$$

Figure 5 shows the derived angular distributions for the first and second transients. In the top chart, the second transient angular distribution is compared with the exhaust-gas angular density distribution derived from the expression for a Brook source [12],

$$N(R_e, \theta) = A \exp[-B(1 - \cos(\theta))]R_e^{-2} \tag{3}$$

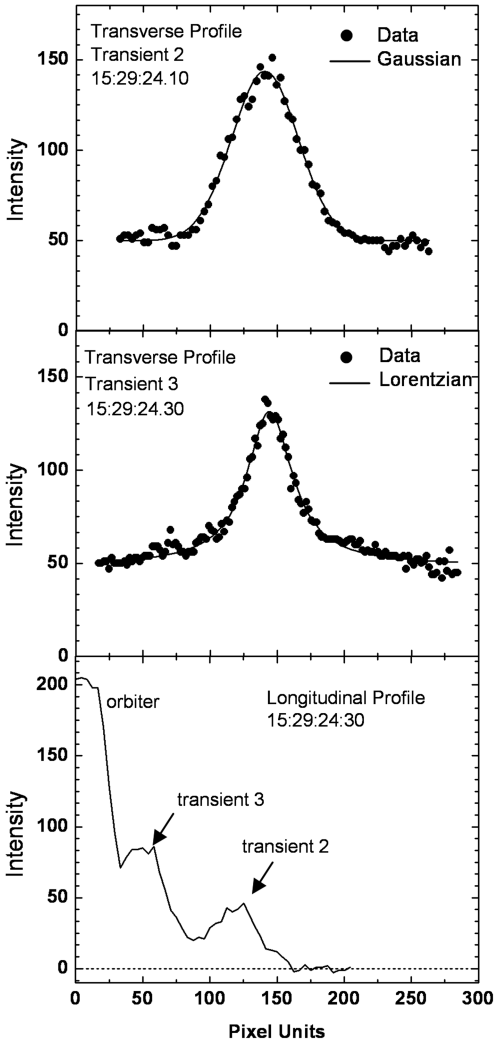

Fig. 4 Transverse and longitudinal intensity profiles of burn 17 transients during indicated times.

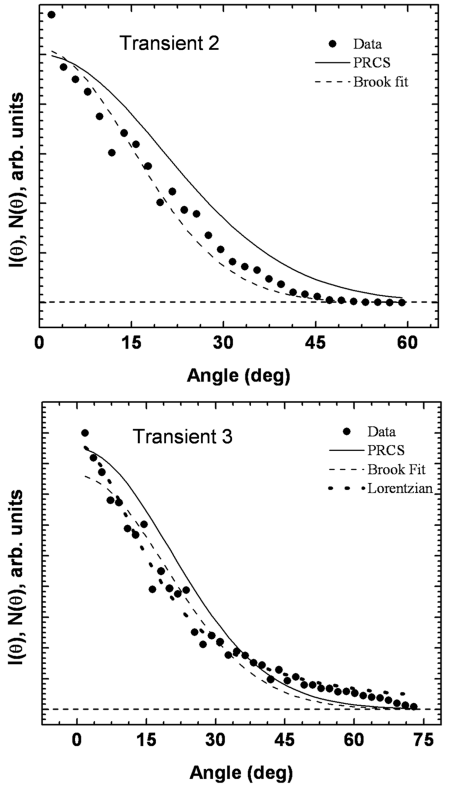

Fig. 5 Comparison of derived transient angular distributions with PRCS Brook flow and parametric fits.

using $B = 8.06$ specified for a PRCS engine. The density is proportional to the emission rate at optically thin conditions. The comparison indicates that the derived angular distribution is slightly narrower than that specified for the PRCS exhaust gases. Also shown is a fit of the Brook parameter B to the observed distribution, yielding $B = 14.4$ for the transient.

The bottom chart in Fig. 5 compares the derived angular distribution of transient 3 to 3 calculated distributions: 1) the PRCS Brook distribution, 2) an attempt to fit a Brook distribution to the data, and 3) a Lorentzian fit. The Lorentzian is given by the expression

$$N(R_e, \theta) = A'(\theta^2 + (\tfrac{1}{2}\Gamma)^2)^{-1} R_e^{-2} \tag{4}$$

The angular parameters B and Γ used for the calculated distributions in Fig. 5 are listed in Table 3, along with the Brook values determined for transient 2 and those applicable to the gaseous exhaust of a PRCS engine. Although a Brook distribution provides an adequate description at angles below 30 deg, at larger angles, there is clearly additional intensity, suggesting that the angular distribution of transient 3 does not obey a Brook distribution. The Lorentzian reproduces the wide-angle signal well in the $I(x)$ distributions (middle frame of Fig. 4); however, a fit of a Lorentzian to the transformed $I(\theta)$ does not capture the distribution correctly at the highest angles (bottom frame of Fig. 5).

To derive more information on the source of the transient signatures, the temporal evolution of the spatially integrated intensity of an entire transient is examined. This was conducted for transient 2 because it is the most intense and compact. Figure 6 shows the dependence of the integrated intensity of the second transient as a function of time following engine shutdown for the F1U engine in pitch-down maneuvers 1 and 17. The intensity was determined following background subtraction by defining the image area of the transient with a polygon. Critical in this effort is the precise determination of background intensities, because errors are additive in the intensity integration. The intensities are normalized with respect to the range (R^{-2}) and atmospheric transmission. In the case of the latter, an average wavelength of 600 nm was assumed. After ~0.5 s, the integrated intensity declines with time. Before 0.5 s, the intensity appears to be constant or rising with time. Examination of the individual pixel intensities indicates that in the case of burn 1, no pixels registered intensities exceeding 200 units before background subtraction, whereas in the case of burn 17, no pixels had intensities exceeding 210 units beyond 0.3 s. It can therefore be concluded that saturation and nonlinearity in the charge-coupled-device (CCD) response are most likely not the source of the varying time dependence of the integrated intensity of the second transient.

The GLO-2 mission on STS-63 that flew in February 1995 obtained spectral data on PRCS engine firings during daytime conditions at similarly low thermospheric densities at an orbital altitude of nearly 400 km [5]. Figure 7 shows spectra recorded during a 3 s PRCS burn and approximately 3 s after the burn. The spectrograph line of sight was nearly parallel to the thrust centerline, and the spectral acquisition times were 2 s. The spectral features in the bottom spectrum, which is on an expanded vertical scale in comparison with the top spectrum, are due to OH, NO, and NH

Table 3 Density (cm^{-3}) and deposition ($g \cdot cm^{-2}$) parameters derived from the angular distribution analysis of the shutdown transients

	Density			Deposition	
	A, cm^{-1}	B	Γ, deg	A, g	A', $g \cdot deg^2$
Gaseous exhaust	1.31×10^{20}	8.07	——	——	——
Transient 2	——	14.4	——	1.12	——
Transient 3	——	8.95	35	1.12	340

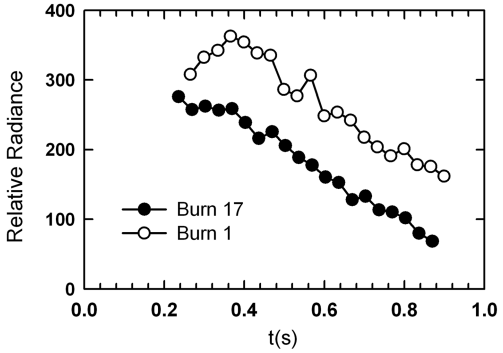

Fig. 6 Range and transmission normalized intensity versus time after shutdown for 2 F1U second transients.

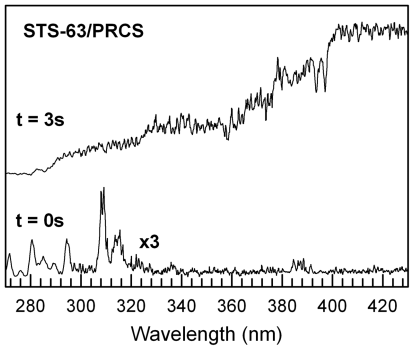

Fig. 7 GLO spectra of exhaust far-field radiance during ($t = 0$) and after a PRCS burn in daylight.

exhaust species (see [5] for an assignment of the bands). The top spectrum exhibits a broad background with increasing intensity with wavelength. The broad feature extends to longer wavelengths. The two sharp features at ~393 and 397 nm are the well-known Ca II K and H lines observed in the solar spectrum. The intense, otherwise featureless, band can therefore be primarily attributed to solar scattering.

Figure 8 shows the time evolution of the integrated intensity of the GLO data between 430 and 460 nm for the same burn that produced the data in Fig. 7, identified as PRCS ram, and an additional PRCS burn, identified as PRCS90. The ram and 90 designations refer to the angle of attack, ram being a burn in which the exhaust vector points into the direction of the velocity vector, and 90 refers to a cross burn. The radiance in Fig. 8 is on an absolute scale,

$$1R = 1 \text{ rayleigh} = 10^6 \text{ photons cm}^{-2} \cdot \text{s}^{-1} \text{ radiated into } 4\pi \text{ sr}$$

and the time corresponds to an estimate of the end of the signal acquisition interval. In the case of the cross burn (PRCS90), the first data point is associated with a spectrum that reveals both exhaust

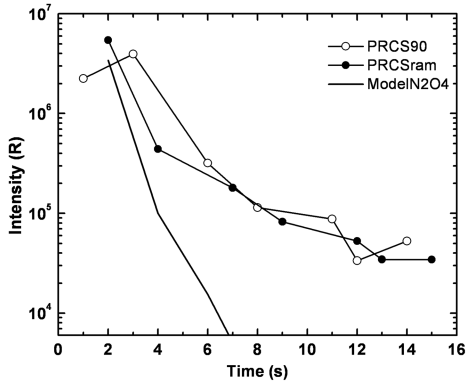

Fig. 8 Comparison between measured (GLO) and calculated (1 μm oxidizer droplet) 430–460 nm band intensity evolution.

spectral features and the significantly more intense continuous radiation. The interval therefore overlaps with $t = 0$.

The two burns at different angles of attack exhibit very similar radiances after shutdown. Given the high altitude, this is expected, as effects due to atmospheric interactions, which are sensitive to the thrust angle of attack, are minimized. The intensity rapidly dims in the first seconds following the end of the burn and then declines at a significantly lower rate. This observation is consistent with the interpretation that solar scattering is the source of transients 2 and 3 that we associate with engine shutdown. The sharp drop in intensity can be related to transient 2, which recedes from the orbiter with a higher velocity, and the fact that the scattering intensity recorded with the GLO instrument scales with R_e^{-2}. The slow decline must be associated with the persistent trails of the slower transient 3. The solid line in Fig. 8 is the calculated intensity evolution of a narrow pulse of 1-μm-diam droplets flying from the GLO sensor at the transient 2 representative speed of 1.6 km $\cdot$ s^{-1}. The model assumes that transient 2 is due to solar scattering from oxidizer condensates, as will be discussed in the next section. The model results are consistent with the early fast decline.

Discussion

Qualitative Interpretation of Transients

The combined ground- and space-based observations of PRCS engine transients in sunlight suggest that the transients arise from solar scattering from condensates in the exhaust. The present data therefore provide an alternative approach to deposition measurements in examining contamination associated with shuttle PRCS engine firings. Solar particle scattering in association with space shuttle experiments has been previously observed in a water vent experiment that occurred during a similar terminator pass over MSSS [13]. In that case, the far-field solar scatter was primarily associated with scattering from submicron-sized particles formed by recondensation of water sublimated from larger ice particles emitted at the orifice. The high velocity of transient 1 formed at engine startup suggests that this transient may be attributable to condensation of some exhaust species.

Condensation of exhaust is typically observed for liquid-oxygen/liquid-hydrogen boosters, as first reported by Kung et al. [14]. Exhaust condensation, however, would imply that the solar scatter would be observable throughout the burn, which is not the case, as demonstrated by the low background levels in the bottom spectrum of Fig. 7 recorded at steady-state burn conditions. Alternatively, it is conceivable that at engine startup, before reaching steady state, mixing of oxidizer and fuel are not complete, leading to unburned droplets that take on the velocity of the exhaust through collisional drag forces. Thus, it is plausible that condensates reside at the exhaust front. Droplets at the exhaust front can also lead to a higher-gas-density region due to evaporation of the droplets in flight. The higher-density gas is then observed through enhanced solar-induced fluorescence intensities. Solar-induced fluorescence should have high yields in the case of NO_2, the primary evaporation product of N_2O_4, given the significant absorption cross sections of NO_2 in the visible spectrum. Meanwhile, the lower sublimation rates and higher heats of sublimation of MMH point to a higher probability of condensate survival for the fuel versus the oxidizer.

It is worth noting that the first transient appears more compact and brighter in the case of the L1U engine used during the roll-left maneuvers. The thrust axis of this engine on the aft left pod points in the direction of the vertical stabilizer of the orbiter. It is possible that interaction between the exhaust and the stabilizer surfaces are the cause of increased brightness of the first transient of this engine. For all other engines used in the present experiments, the exhaust does not interact directly with orbiter surfaces.

The shutdown transients are most likely due to small amounts of oxidizer and fuel present in the vacuum manifold between the tank valves and the combustion chamber. The manifold volume of a space shuttle PRCS engine is ~5 cm^{-3} for the oxidizer and ~8 cm^{-3} for the fuel. When the oxidizer and fuel valves are turned off

simultaneously, the oxidizer and fuel in the vacuum manifold are no longer pressurized. They escape the manifold through their vapor pressure. The more volatile oxidizer can then be expected to vent into the combustion chamber at higher rates than the fuel, which is also considerably more viscous. This interpretation implies that transient 2 is due to oxidizer condensates and transient 3 is attributable to the MMH fuel.

The size of the condensates dictates both the scattering intensities and transient velocities. If all transients are due to condensates, their terminal velocities, listed in Table 2, are governed by their interaction with the expanding gaseous species. At a low size limit, particles are expected to take on the terminal velocity of the gas. This is demonstrated in Fig. 9, which plots the particle velocity as a function of distance from the nozzle for 3 particle sizes. The calculations assume that particles are expanded with the steady-state exhaust of a PRCS engine at the exit ($\sim$3 km s^{-1}) and that full gas accommodation occurs (i.e., every gas–particle collision leads to sticking of the gas species). This corresponds to the conditions for maximum acceleration, and thus the determined terminal velocities must be regarded as upper limits. The model determines that condensates of a 0.1 μm diameter experience no velocity slip, whereas 1- and 10-μm-diam particles reach asymptotic velocities of 2850 and 2100 m/s, respectively. In the case of the startup transient (first transient), the condensates would have essentially the terminal velocity of the exhaust gases in the collisionless regime. Thus, the calculations in Fig. 9 suggest that if the first transient is due to condensates, the average particle/droplet size is significantly below 1 μm. A subsequent discussion of the Mie-scattering properties demonstrates that the scattering cross sections decline rapidly with particle size in this size regime, which would be consistent with the low intensity. However, given the available information, it cannot be definitively concluded whether the first transient is due to fluorescence from a higher-gas-density region or direct scattering from condensate particles. The calculations in Fig. 9 do not apply directly to the shutdown transients (transients 2 and 3) because the condensates are not entrained in the same steady-state PRCS exhaust-gas flow.

We can interpret the second transient as being due to submicron-particle condensates. In this interpretation, a very lean propellant mixture at shutdown leads to a lower-temperature expansion and terminal velocities of $\sim$1.6 km $\cdot$ s^{-1}. The exhaust gases resulting from the leaner combustion would be expected to accelerate the oxidizer droplets to lower velocities than those produced at optimal combustion conditions. Alternatively, the velocities can be explained by complete and instantaneous vaporization of the liquid manifold oxidizer when striking the hot combustion-chamber walls. Given the $\sim$7.6 g mass of the manifold oxidizer and assuming a density of 1.52 g $\cdot$ cm^{-3} and a chamber volume of $\sim$320 cm^{-3}, complete vaporization should produce chamber pressures of several

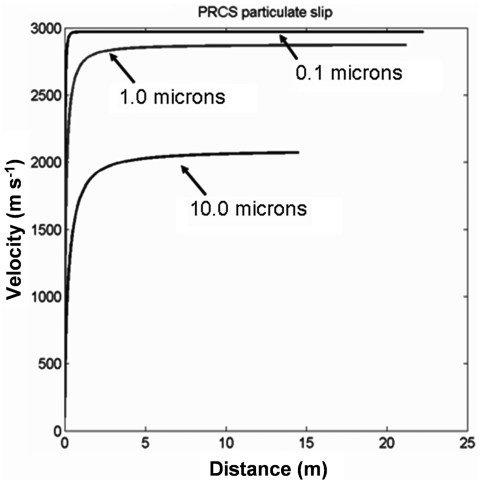

Fig. 9 Particle velocity as a function of axial nozzle distance for 3 particle sizes.

atmospheres. Thus, the transient may be associated with a hard expansion of purely gaseous oxidizer that leads to recondensation. In such an expansion, the thermal energy (consisting of translational, rotational and vibrational energy of the NO_2 gas) gets effectively channeled into translational energy. The observed transient velocity of 1.63 km $\cdot$ s^{-1} would then be consistent with a chamber wall temperature of $\sim$1600 K. At this temperature, the chamber pressure would be $\sim$60 atmospheres if the chamber had no escape aperture.

The less volatile MMH appears more like a protracted flow of liquid than a compact cloud. Because of the lower vapor pressure, it can be expected that the pressure due to evaporation of the fuel is significantly lower than for the oxidizer, which is consistent with the significantly lower velocity measured for the leading edge of transient 3.

Evolution of Condensates Injected into Space

In the present section, the transient condensates are modeled in a more quantitative way. Focusing on transient 2, the decline in integrated cloud intensity as a function of time with respect to engine shutdown, shown in Fig. 6, is indicative that the oxidizer condensates are losing mass and shrinking in radius through sublimation. This is analogous to the observations made during space shuttle water releases [13]. As described by Kofsky et al. [13], the size and temperature evolution of a droplet in space can be obtained by integrating the heat balance equation:

$$\dot{Q}(r,T) = \frac{4\pi}{3} r^3 \rho C_p(T) \dot{T} = \dot{Q}_{\text{sun}}(r) + \dot{Q}_{\text{Earth}}(r) - \dot{Q}_{\text{rad}}(r,T) - \dot{Q}_{\text{sub}}(r,T) \tag{5}$$

where $\dot{Q}(r,T)$ is the particle heat gain or loss rate, which is given by the sum of heating by solar and Earthshine radiation and the cooling through radiative and evaporative or sublimation cooling; $\rho = 1.52$ g cm^{-3} is the density; and $C_p(T)$ is the temperature-dependent specific heat (constant pressure) of N_2O_4. The heating terms are given by the solar and Earthshine absorption expressions:

$$\dot{Q}(r) = \int \varepsilon(r,\nu)\Omega r^2 P(\nu, T_i)\mathrm{d}\nu \tag{6}$$

where Ω is the solid angle subtended by the Earth ($\sim 1.4\pi$ sr at 335 km) or sun (6.8×10^{-5} sr), and $P(\nu, T_i)$ is the Planck radiation function with respect to the frequency ν, where $T_i = 280$ and 5800 K for the Earth and sun, respectively. The radiative loss term is given by

$$\dot{Q}_{\text{rad}}(r,T) = 4\pi \int \varepsilon(r,\nu) r^2 P(\nu, T_i)\mathrm{d}\nu \tag{7}$$

and the sublimation term is calculated from

$$\dot{Q}_{\text{sub}}(r) = 4\pi r^2 \rho \Delta H_{\text{sub}} \dot{r} \tag{8}$$

where $\Delta H_{\text{sub}} = 590$ J/g is the average heat of sublimation over the pertinent temperature range. The emissivities were calculated from the indices of refraction reported by Roux and Woodward [15] using standard Mie theory [16]. Although Roux and Woodward [15] do not report indices below wavelengths of ~ 2 μm, we assume no significant variation of the real index of refraction at shorter wavelengths, and we estimate the complex index of refraction from the absorption cross section of NO_2 at 600 nm. This leads to an estimated refractive index of $1.53 \pm 0.005i$ at the visible wavelengths of observation. Equation (5) is then coupled with the expression for change in radius by sublimation as expressed through the temperature-dependent vapor pressure [13]. Parameters for both N_2O_4 and MMH used for the calculation of $r(t)$ and $T(t)$ are shown in Table 4.

The bottom two charts in Fig. 10 show the time evolution of the diameter $D = 2r$ and temperature of the original 1-, 0.1-, and 0.02-μm-diam N_2O_4 particles exposed to sunlight at an altitude of $\sim$335 km. The diameter is plotted as its ratio with respect to the

Table 4 Parameters used for fuel and oxidizer particle evolution simulations

	N_2O_4	$CH_3N_2H_3$ (MMH)
ρ	1.52	0.88
C_p	$-0.11 + 1.23 \times 10^{-2}T + 5.58 \times 10^{-5}T^2 + 1.09 \times 10^{-7}T^3$	$2.74 - 7.24 \times 10^{-5}T + 2.48 \times 10^{-6}T^2$
ΔH_{sub}	590	875
$\log_{10}P_{vap}(T)$	$9.82 - 2332T^{-1} + 8.46 \times 10^4T^{-2}$	$7.11 - 1104.6T^{-1} + 1.52 \times 10^5T^{-2}$

initial diameter D_0. The initial temperature was chosen to be 250 K. This is near the melting point of N_2O_4, which depends significantly on the content of NO. Our calculations show that it takes less than 1 ms to dissipate the N_2O_4 heat of fusion of 14.7 kJ/mol, and so neglecting the phase transition in the present calculations only introduces a minor error. The charts demonstrate that the initial stage is dominated by sublimation, leading to very rapid cooling (within ~20 ms) to below 150 K. During this period, the diameter of the particle significantly decreases below $D/D_0 = 0.7$. After the first ~200 ms, the temperature and size of the particles declines only slowly as the particle reaches a steady state in which the dominant cooling mechanism is radiative and the predominant heating mechanism is Earthshine absorption.

The top chart in Fig. 10 plots the predicted relative scattered sunlight intensity as a function of time for the subject particle at the scattering angle $\phi = 112$ deg ($\varphi = 180$ deg) that was effective during burn 1. The intensities for the different sizes are brought to the same scale by normalizing with respect to the intensity at 0.3 s, which is approximately the time after shutdown at which the oxidizer cloud intensity can be determined. The scattered intensity from a single particle is calculated from

$$I(\varphi) = \int_0^\infty \mathrm{d}\nu\, g(\nu) F_S(\nu) \sigma(\nu, r, \varphi) \tag{9}$$

where $g(\nu)$ incorporates the spectral atmospheric transmission and sensor sensitivity, $F_S(\nu)$ is the solar flux, and $\sigma(\nu, r, \varphi)$ is the Mie-scattering differential cross section. The result is compared with the integrated intensity evolution for burn 1 following scaling of the experimental data. Although the observed decline in intensity with time is recovered by the calculations, it is seen that the observed intensity declines more rapidly than the 3 calculated curves. The calculations indicate an increasing decline as the particle size is lowered from 1 to 0.1 μm, despite a decreasing decline in diameter. This is indicative of the transitional scattering regime between geometric and Rayleigh scattering at the respective particle sizes. The geometric scattering intensities are proportional to r^2, whereas in the Rayleigh regime they are proportional to $\sim r^4$. The decline in intensity, however, is lowest for the smallest particle size of 0.02 μm. This can be attributed to the very small decrease in size due to the very low evaporation rates at the low near-steady-state temperature of ~90 K of these particles.

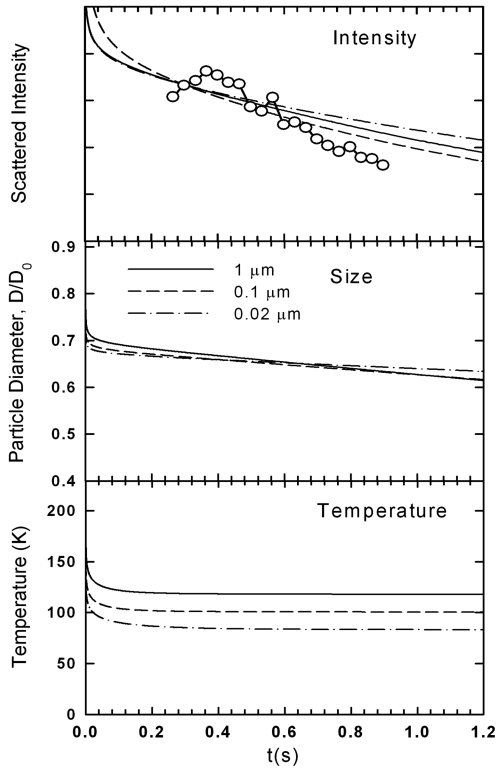

Fig. 10 Evolution of oxidizer particle size, temperature and intensity and comparison with burn 1 intensity data.

The significant pressures produced by the evaporating oxidizer after shutdown, discussed in the previous section, raise the possibility that the oxidizer transient is due to submicron-sized condensates formed in the expansion of the gas. It is therefore possible that the initial increase or near-constant intensity seen in Fig. 6 may be due to continued condensate growth up to ~0.3 s after shutdown. This explanation implies that the accommodating gas-condensate collision rate exceeds the rate of evaporative loss.

The present calculations must be considered highly approximate for several reasons: first and foremost is the assumption of a single particle size. Furthermore, the lack of absorption coefficients for solid N_2O_4 at wavelengths exceeding 2 μm required an estimate, which in itself could explain the discrepancy between observation and experiment. Finally, the calculations assume particles consisting of smooth spheres. As discussed by Kofsky et al. [13], simple Mie-scattering calculations such as the one presented here do not account for particle albedo reduction due to surface roughening that may be caused by sublimation. This could also account for the more rapid decline in intensity observed in the experiments.

Condensate Deposition Rates

The STS-115 observations reported here have allowed the first determination of the angular distribution of condensates in the exhaust of a PRCS engine. Next, we relate these angular distributions to previous centerline deposition rates and suggest values for the deposition rate as a function of distance and angle. Previous experiments have quantified deposition rates on the thrust centerline [1,2]. In the work by Soares et al. [2], a deposition rate of 1.282×10^{-5} g · cm^{-2} · s^{-1} was derived from the study of 20 80 ms PRCS engine firings at a distance of 10.58 m. The deposition rate was derived assuming a total engine firing duration of 1.6 s. From the Brook equation for the engine-exhaust number densities and the parameters in Table 3, we can determine an estimate for the total centerline exhaust particle flux F at a distance of 10.58 m from

$$F = N(R_e) v_e \tag{10}$$

where $v_e = 3.5$ km · s^{-1} is the far-field exhaust velocity, and $N(R_e)$ is the Brook number density at the axial distance R_e [9,10]. Assuming an average molecular mass of 23 atomic mass units based on the known exhaust constituent distribution [10], a mass flux $F \cdot m$ of 1.56×10^{-3} g · cm^{-2} · s^{-1} is derived. Thus, the mass flux associated with the deposition registered by the quartz crystal microbalance (QCM) in the study by Soares et al. [2] represents approximately 0.8% of the exhaust mass flux.

This suggests that the QCM deposition may be associated with the presently discussed transient condensate fluxes. If this were the case, the deposition rate relates to the number of engine burns instead of

the burn lengths and amounts to approximately 1 $\mu g \cdot cm^{-2}$ per burn at the QCM. By relating the derived condensate mass flux fraction at the QCM to the total exhaust mass ejected during a single 0.08 s burn, which can be derived from the known PRCS engine mass flow of 1.4 $kg \cdot s^{-1}$, the QCM measurements suggest that 1 g of condensates survive per PRCS burn at a nozzle distance of 10.58 m. This quantity is consistent with the propellant mass in the engine vacuum manifold at shutdown. Given the previously mentioned manifold volumes of $\sim$5 cm^{-3} for the oxidizer and $\sim$8 cm^{-3} for the fuel and given the densities of 1.52 $g \cdot cm^{-3}$ and 0.88 $g \cdot cm^{-3}$ for N_2O_4 and MMH, respectively, 7.6 and 7 g of unpressurized oxidizer and fuel, respectively, are in the vacuum manifold at engine shutdown. Thus, if the QCM signal is entirely due to the observed transients, less than 10% of the shutdown transient material is in condensed form at a distance of $\sim$10 m, assuming that the QCM measurements efficiently detected it. The condensate evaporation studies applied to oxidizer particles discussed in the previous subsection indicates that particles with radii between 0.01 and 10 μm lose approximately 60–70% of their mass due to evaporation after a flight time corresponding to a flight distance of 10.58 m at the average oxidizer-transient velocity. Calculations conducted for MMH fuel, on the other hand, indicate that only approximately 30% mass loss occurs during the same flight distance.

The present estimates based on the QCM results must be regarded as lower bounds, given the relatively high ejection velocities, particularly of the oxidizer transient. The associated hypervelocity impacts at the QCM could result in considerable ejection of material, resulting in lower readings. It can be expected that the QCM detects substantially more fuel than oxidizer because of the significantly lower velocities of the fuel transient, which we have only determined for the first burst and which can be expected to be lower during the persistent "dribble" stages of the transient. An x-ray photoelectron spectroscopy analysis of impact craters due to condensates in the PRCS exhaust indicated high-oxidation-state nitrogen, possibly attributable to MMH-nitrate [2], thereby suggesting effects due to both fuel and oxidizer. The lack of information on the size distributions of oxidizer and fuel particles prevents quantifying the optical signals in terms of total condensate mass. However, the time dependence of the GLO intensities associated with condensate solar scatter and the evolution of transients observed in the STS-115 MAUI data indicate that the time-integrated solar-scattered signal due to fuel is more than a factor of 3 more intense than that of the oxidizer, which appears only as a narrow, compact feature.

A Brook parameter for mass deposition as a function of nozzle distance and angle is provided in Table 3 based on the centerline results of Soares et al. [2] of 1 $\mu g \cdot cm^{-2}$ per burn at 10.58 m and the assumption that the results reported by Soares et al. are directly related to the observed transients 2 and 3. The Brook model does not take the high-angle tail of transient 3 into account. We therefore also provide suggested parameters for the Lorentz-type distribution, assuming that the condensate deposition is primarily due to the fuel (transient 3). The high-angle tail may be a consequence of fuel film cooling of the nozzle, causing liquid ejection at larger angles.

Soares et al. [2] observed and quantified craters formed on aluminum and Kapton samples exposed to 84 PRCS and 17 vernier reaction-control-system engine firings. Most of the crater diameters on aluminum were less than 10 μm in diameter. Studies that relate crater size to particle diameter find that at impact velocities of around 2 $km \cdot s^{-1}$, craters tend to be similar to or less than the particle diameter, whereas at 1 $km \cdot s^{-1}$, the crater diameters drop significantly below the particle diameter [17,18]. In the case of the aluminum sample, the most abundant crater sizes were less than 4 μm. Relating the number of such craters, 449 mm^{-2}, to similarly sized particles leads to the conclusion that the mass deposition associated with the craters is approximately 2 orders of magnitude smaller than that detected by the QCM without taking material ejection into account. It is possible that the fast-exhaust species associated with transient 1 may be primarily responsible for the cratering. Unfortunately, that transient was too weak and its observation time was too short to allow a meaningful analysis.

Conclusions

Imagery of PRCS engine far-field exhaust was analyzed for 22 attitude-control firings during an STS-115 terminator pass over the Maui Space Surveillance Site (MSSS). This imagery was interpreted in terms of sunlight scattering of exhaust condensates. Each firing is associated with three transients: one weak transient at engine startup and two intense transients at engine shutdown. An analysis of the transient velocities finds that the startup transient is close to the freestream exhaust velocity of 3 $km \cdot s^{-1}$, and the two shutdown transients have average velocities of 1.63 and 0.71 $km \cdot s^{-1}$, respectively. Although the startup transient is attributed to initially unburned propellant in either a condensed or gaseous state, the shutdown transients are attributed to oxidizer and fuel solid particles. The compact shutdown oxidizer transient appears before the fuel transient due to its higher vapor pressure. The shutdown fuel transient, on the other hand, exhibits an initial burst followed by a persistent dribble trail. The time dependence of the shutdown oxidizer transient's integrated intensity suggests that particles of approximately 1 μm diameter or smaller are the source of the observed solar scattering. From the imagery, the angular distribution of the PRCS exhaust condensates is derived. An analysis of the angular distribution of the shutdown oxidizer transient demonstrates that it is well described by a Brook source distribution with an angular spread slightly narrower than that specified for the gaseous exhaust. A similar analysis on the initial burst of the shutdown fuel transient indicates that a Brook distribution does not capture considerable material at large angles.

The present analysis in context with axial deposition measurements [2] of a shuttle PRCS engine in space suggests that at least 10% of the propellant manifold volume is ejected as condensates at shutdown. This assumes that the deposition signals are caused by the shutdown transients. The higher vapor pressure and associated sublimation rates of the oxidizer suggest that condensate release and deposition are more important for the MMH fuel. This is consistent with spaceborne measurements using the GLO instrument, for which the effects due to condensate solar scatter are observed beyond 10 s following a PRCS burn. The extended solar scattering signals are attributed to the persistent MMH dribble.

Acknowledgments

This work has been initiated and partially funded by the U.S. Air Force Office of Scientific Research under tasks 2301HS and 02VS06 (Kent Miller, program manager). L. S. Bernstein and M. Braunstein of Spectral Sciences, Inc., acknowledge support from the U.S. Air Force Research Laboratory under contract FA8718-05-C-0077 (Y. Chiu, program manager). The authors are highly indebted to Albert Meza, Darrin Walker, and James McLeroy of the U.S. Department of Defense Space Test Program at NASA Johnson Space Flight Center for a masterful integration of the Maui Analysis of Upper-Atmospheric Injections (MAUI) Space Experiment. P. F. Sydney is grateful for invaluable assistance by Lewis Roberts and Kris Hamada. The authors are indebted to Paul Kervin and Mark Bolden at the U.S. Air Force Maui Optical and Supercomputing site (AMOS) for their support and advocacy on behalf of the MAUI effort. The authors wish to thank Lonnie Schmidt of Johnson Space Center for providing valuable engine parameters.

References

[1] Koontz, S., Ehlers, H., Pedley, M., Hakes, C., and Cross, J., "Shuttle Primary Reaction Control System (PRCS) Engine Exhaust Plume Contamination Effects: The Shuttle Plume Impingement Experiment (SPIE), STS-52," 31st Aerospace Sciences Meeting and Exhibit, Reno, NV, AIAA Paper 93-0618, Jan. 1993.

[2] Soares, C., Barsamian, H., and Rauer, S., "Thruster Plume Induced Contamination Measurements from the PIC and SPIFEX Flight Experiments," *Optical System Contamination: Effects, Measurements, and Control*, Vol. 4774, No. 1, Society of Photo-Optical Instrumentation Engineers, Bellingham, WA, 2002, pp. 199–209.

[3] Broadfoot, A. L., Sandel, B. R., Knecht, D. J., Viereck, R. A., and Murad, E., "A Panchromatic Spectrograph with Supporting

Monochromatic Imagers," *Applied Optics*, Vol. 31, No. 16, 1992, pp. 3083–3096.

[4] "The Arizona Airglow Experiment (GLO)," *Shuttle Payload Program* [online database], http://glo.lpl.arizona.edu/glo [retrieved 17 Nov. 2008].

[5] Bernstein, L. S., Chiu, Y., Gardner, J, A., Broadfoot, A. L., Lester, M. I., Tsiouris, M., Dressler, R. A., and Murad, E., "Molecular Beams in Space: Sources of OH(A-X) Emission in the Space Shuttle Environment," *Journal of Physical Chemistry A*, Vol. 107, No. 49, 2003, pp. 10695–10705. doi:10.1021/jp035143x

[6] Bernstein, L. S., Braunstein, M., Broadfoot, A. L., Dimpfl, W. L., Dressler, R. A., Chiu, Y.-h., Gardner, J. A., and Murad, E., "Far-Field Spectral Analysis of a Space Shuttle Vernier Reaction Control System Firing," *Journal of Spacecraft and Rockets*, Vol. 43, No. 6, 2006, pp. 1370–1376. doi:10.2514/1.21252

[7] Viereck, R. A., Murad, E., Knecht, D. J., Pike, C. P., Bernstein, L. S., Elgin, J. B., and Broadfoot, A. L., "The Interaction of the Atmosphere with the Space Shuttle Thruster Plume: The NH(A-X) 336 nm Emission," *Journal of Geophysical Research*, Vol. 101, No. A3, 1996, pp. 5371–5380. doi:10.1029/95JA03635

[8] Knecht, D. J., Murad, E., Viereck, R., Pike, C. P., Broadfoot, A. L., Anderson, E. R., Hatfield, D. B., Stone, T. C., and Sandel, B. R., "The Arizona Airglow Experiment as Flown on Four Space Shuttle Missions," *Advances in Space Research*, Vol. 19, No. 4, 1997, pp. 627–630. doi:10.1016/S0273-1177(97)00155-5

[9] Pickett, J. S., Murphy, G. R., Kurth, W. S., Goertz, C. K., and Shawhan, S. D., "Effects of Chemical Releases by the STS-3 Orbiter on the Ionosphere," *Journal of Geophysical Research*, Vol. 90, No. A4, 1985, pp. 3487–3497. doi:10.1029/JA090iA04p03487

[10] Viereck, R. A., Bernstein, L. S., Mende, S. B., Murad, E., Swenson, G. R., and Pike, C. P., "Visible Spectra of Thruster Plumes from the Space Shuttle Primary Reaction Control System," *Journal of Spacecraft and Rockets*, Vol. 30, No. 6, 1993, pp. 724–730. doi:10.2514/3.26378

[11] Fan, L. S., and Squire, W., "Inversion of Abel's Integral Equation by a Direct Method," *Computer Physics Communications*, Vol. 10, No. 2, 1975, pp. 98–103. doi:10.1016/0010-4655(75)90076-4

[12] Brook, J. W., "Far Field Approximation for a Nozzle Exhausting into a Vacuum (Density Profiles in Far Field of Reaction Control System Plumes in Vacuum Obtained by Method Eliminating Difficulties Encountered by Continuum Method)," *Journal of Spacecraft and Rockets*, Vol. 6, No. 5, 1969, pp. 626–628. doi:10.2514/3.29626

[13] Kofsky, I. L., Rall, D. L. A., Maris, M. A., Tran, N. H., Murad, E., Pike, C. P., Knecht, D. J., Viereck, R. A., Jr., Stair, A. T., and Setayeh, A., "Phenomenology of a Water Venting in Low Earth Orbit," *Acta Astronautica*, Vol. 26, No. 5, 1992, pp. 325–347. doi:10.1016/0094-5765(92)90079-X

[14] Kung, R. T. V., Cianciolo, L., and Myer, J. A., "Solar Scattering from Condensation in Apollo Translunar Injection Plume," *AIAA Journal*, Vol. 13, No. 4, 1975, pp. 432–437. doi:10.2514/3.49725

[15] Roux, R. A., and Woodward, B. E., "Infrared Optical Properties of Solid Monomethyl Hydrazine, N_2O_4, and N_2H_4 at Cryogenic Temperatures," *Journal of the Optical Society of America*, Vol. 73, No. 9, 1983, pp. 1181–1188.

[16] van_de_Hulst, H. C., *Light Scattering by Small Particles*, Dover, New York, 1981.

[17] McDonnell, T., McBride, N., and Green, S. F., "Near Earth Environment," *Interplanetary Dust*, edited by E. Gruen, B. A. S. Gustafson, S. F. Dermott, and H. Fechtig, Springer, New York, 2001, pp. 163–232.

[18] Burchell, M. J., Cole, M. J., McDonnell, J. A. M., and Zarnecki, J. C., "Hypervelocity Impact Studies Using the 2 MV van de Graaff Accelerator and Two-Stage Light Gas Gun of the University of Kent at Canterbury," *Measurement Science and Technology*, Vol. 10, No. 1, 1999, pp. 41–50. doi:10.1088/0957-0233/10/1/011

I. Boyd
Associate Editor